Nuclear Engineering and Design 414 (2023) 112600

Contents lists available at ScienceDirect

Nuclear Engineering and Design

journal homepage: www.elsevier.com/locate/nucengdes

Validation and uncertainty analysis of ASTEC in early degradation phase against QUENCH-06 experiment

Pietro Maccari [a,*], Andrea Bersano [b], Stefano Ederli [c], Fabrizio Gabrielli [d], Fulvio Mascari [b,*]

[a] ENEA, FSN-ING-SIS, C.R. Brasimone, Camugnano, Italy
[b] ENEA, FSN-SICNUC-SIN, Via Martiri di Monte Sole 4, Bologna, Italy
[c] ENEA, FSN-SICNUC-SIN, Casaccia, Via Anguillarese 301, Italy
[d] KIT, Hermann-von-Helmholtz-Platz, 1, Karlsruhe, Germany

ARTICLE INFO

Keywords:
ASTEC
Severe accident
QUENCH
Accuracy
Uncertainty

ABSTRACT

Severe Accident (SA) integral codes, such as the Accident Source Term Evaluation Code (ASTEC) developed by IRSN, are used to simulate the phenomena occurring during accident progression in Nuclear Power Plants (NPPs) up to the source term evaluation. Code validation against experimental data is fundamental to carry out deterministic safety analysis and apply these codes to NPPs. In addition, in the Best Estimate Plus Uncertainty (BEPU) framework, the quantification of the results uncertainty is needed. In the framework of the IAEA CRP I31033 "Advancing the State-of-Practice in Uncertainty and Sensitivity Methodologies for Severe Accident Analysis in Water-Cooled Reactors", the QUENCH test-6 experiment, conducted at KIT, has been selected to develop an uncertainty analysis using the ASTEC v2.2b code. The accuracy of the best-estimate ASTEC simulation was evaluated with the Fast Fourier Transform Based Method (FFTBM) against the experimental data. Then, the uncertainty of the code results was quantified by using the probabilistic propagation of input uncertainties method, through the coupling of ASTEC with RAVEN (Risk Analysis and Virtual Environment). Beyond identifying the main sources of uncertainty affecting the simulated test, the outcomes of the work also include some general discussion on the uncertainty propagation in a SA sequence.

1. Introduction

Severe Accident (SA) integral codes are developed to simulate an accidental progression in Nuclear Power Plants (NPPs) up to the source term evaluation. These numerical codes, such as ASTEC (Chatelard et al., 2016), MELCOR (Humphries et al., 2015) and MAAP (FAI/13-0801, 2013), should be able to predict all the main physical phenomena involved in a SA progression. One key aspect of code application is the validation through the comparison of the code results against the data measured in experimental facility. This can be carried out by an independent code user (Code Independent Qualification) and it is finalized at evaluating the code accuracy through qualitative and a quantitative methodologies (Mascari et al., 2015).

In addition, in the Best Estimate Plus Uncertainty (BEPU) framework, there is the need to quantify the uncertainty of the code results (D'Auria et al., 2008). In fact, Uncertainty Quantification (UQ) methods are well established in the field of nuclear thermal-hydraulics, see as example (D'Auria et al., 2008; OECD/NEA/CSNI, 2007; Baccou, 2020; OECD/NEA/CSNI, 2011; OECD/NEA/CSNI, 2016), and they have begun to be applied in the SA field. Some examples of UQ applications in the SA field can be found in (Herranz et al., 2021; Mascari et al., 2023; Coindreau, 2023; Mascari et al., 2022; Brumm et al., 2022; Mascari et al., 2022).

The present paper describes the activity carried out in the framework of the International Atomic Energy Agency (IAEA) Coordinated Research Projects (CRP) - I31033 "Advancing the State-of-Practice in Uncertainty and Sensitivity Methodologies for Severe Accident Analysis in Water-Cooled Reactors" (https://www.iaea.org/projects/crp/i31033), based on the QUENCH test-6 experiment. QUENCH facility is being operated at the Karlsruher Institut fur Technologie (KIT) to characterizing the behavior of hot and pre-oxidized fuel rods in quenching conditions (e.g. fast cooling due to direct contact with water). On December 13th 2000, test-6 was performed, in which 21 fuel rods simulators and 4 corner rods were heated up and quenched by a bottom water injection in a Argon - Steam environment (Sepold et al., 2004).

The first part of the study is focused on the validation of the ASTEC (Accident Source Term Evaluation Code) models for early-degradation phenomena and hot core quenching, against the test-6 experimental

* Corresponding authors.
E-mail addresses: pietro.maccari@enea.it (P. Maccari), fulvio.mascari@enea.it (F. Mascari).

https://doi.org/10.1016/j.nucengdes.2023.112600
Received 28 July 2023; Received in revised form 11 September 2023; Accepted 13 September 2023
Available online 18 September 2023

Nomenclature

AA	Average Amplitude
ASTEC	Accident Source Term Evaluation Code
BEPU	Best-Estimate Plus Uncertainty
CRP	Coordinated Research Projects
FFTBM	Fast Fourier Transform Based Method
FOM	Figures Of Merit
IAEA	International Atomic Energy Agency
IRSN	Institut de Radioprotection et de Sûreté Nucléaire
HPC	High Performance Computing
KIT	Karlsruher Institut fur Technologie
LWR	Light Water Reactor
NPPs	Nuclear Power Plants
PDF	Probability Density Function
PhW	Phenomenological Windows
RAVEN	Risk Analysis and Virtual Environment
SA	Severe Accident
STD	Standard Deviation
UQ	Uncertainty Quantification
WF	Weighted Frequency

The work has the purpose of providing outcomes regarding the code capabilities in the simulation of the SA early-degradation phenomena involved in the experimental test, also highlighting code models strengths and challenges. Indeed, the direct comparison of the results and the application of FFTBM against the experimental data provide a characterization of the accuracy of the best-estimate simulation results. Additionally, the uncertainty affecting the calculation is investigated through the application of an UQ methodology and, as a further outcome, the input uncertain parameters manly correlated with the selected Figures Of Merit (FOM) are identified.

Furthermore, the study wants to explore the application of the BEPU methodology to SA code simulations, highlighting challenges and perspectives. In this framework, a cliff-edge effect related to local material melting and relocation has been identified.

2. Description of the QUENCH test-6 experiment

The QUENCH experimental facility, hosted in the Institute for Applied Materials Applied Materials Physics (IAM-AWP) of KIT, was designed to investigate the behavior of hot and pre-oxidized LWR fuel in quenching conditions. The test-6 was aimed at investigating the injection of water from the bottom of the hot core as accident management measure. This test has been used as an OECD - ISP (ISP-45) for blind and open calculations to assess SA codes (Sepold et al., 2004).

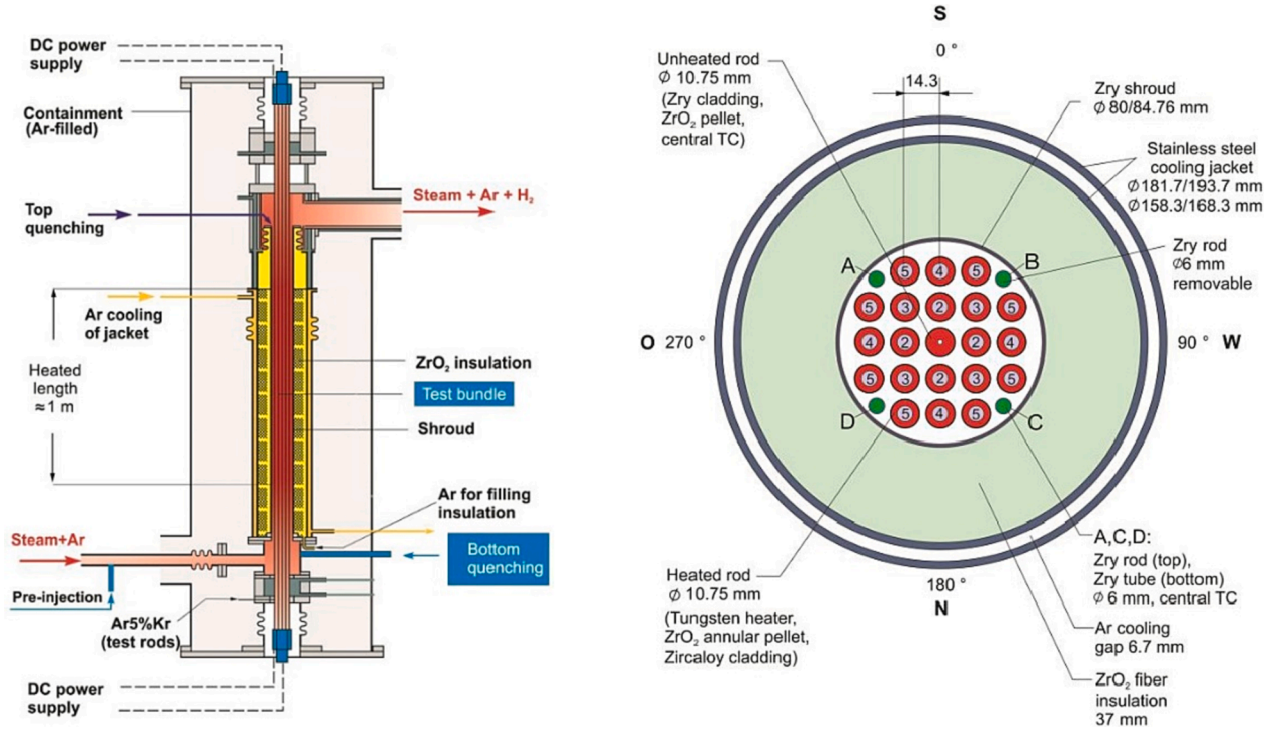

Fig. 1. Vertical section of the facility (left) and horizontal section of the test-section (right) in QUENCH test-6 arrangement (Sepold et al., 2004).

data. Previous studies regarding ASTEC code and modelling of QUENCH-6 can be found in (Gabrielli et al., 2019; Kaliatka et al., 2014). In particular, the ICARE and the CESAR modules of ASTEC code v2.2 beta (study carried out with ASTEC V2, IRSN all rights reserved, [2022]) were used for the modelling and simulation of the QUENCH test-6 experiment. The results of the best-estimate simulation are compared against the experimental data provided by KIT and the accuracy of the code is quantitatively evaluated by means of the Fast Fourier Transform Based Method (FFTBM; Ambrosini, 1990; Bersano et al., 2020). Then, the UQ study is performed to characterize the uncertainty affecting the code simulation results.

2.1. QUENCH test-6 set-up

The test-section of the QUENCH facility hosts the rod bundle schematically shown in Fig. 1. In the test-6, the bundle includes 21 fuel rod simulators surrounded by a shroud of Zircaloy, a fiber insulation and an external stainless-steel cooling-jacket. 20 of the 21 fuel rod simulators are electrically heated over a length of 1024 mm by means of a tungsten heater in the center of the rods, which is surrounded by ZrO_2 pellets and the Zr cladding. The unheated rod is placed at the center of the bundle, filled only with ZrO_2 pellets. Above the heated zone level there is no insulation and the cooling jacket is cooled by a water flow, forcing the

Table 1
Main events characterizing the QUENCH test-6 sequence (Sepold et al., 2004).

Time (s)	Event	PhW
0	Start of experiment; bundle at T~870 K; Ar and steam bottom injection (~3 g/s both).	Pre-oxidation
30	Start of heating up to ~1473 K	
1965	Start of steady temperature oxidation at ~1473 K	
6011	Start of heat up phase	Heating-up
6620	Extraction of corner rod B from the bundle	
~7200	Onset of temperature escalations and of significant H_2 production	
7179	Argon injection moved to the upper plenum; shutoff of steam injection; start of quenching with the water "pre-injection" (4 L in 5 s); rod failure in the experiment.	Quenching
7180	Shroud failure in the experiment	
7205	Start of electric power reduction from 18.2 kW to 3.9 kW	
7215	Start of water main injection (time-dependent mass flow rate)	
7221	Electric power at 3.9 kW	
7431	Electric power shutoff	
7434	Main water at zero	
9000	End of the test	

maximum axial temperature of the system downward. 4 Zr rods (corner rods) are located at the corners of the bundle, these hosts most of the instrumentation. The section is bounded by top and bottom sealing plates and the rods are supported by spacer grids. Superheated steam mixed with argon enters from the bottom and moves upwards along the bundle. The injected gases and the H_2 eventually generated exit at the top end, where a mass spectrometer and other instrumentations are located. The quenching water enters in the test-section through a bottom line. A more detailed description of the QUENCH test-6 arrangement can be found in (Sepold et al., 2004).

2.2. QUENCH test-6 test conduct

The experimental sequence has been divided in 3 main Phenomenological Windows (PhW). These are defined by the fluids injections and the variation of electrical power applied:

- Pre-oxidation PhW: from the start of the sequence (0 s) up to 6011 s, during which the electric power applied is increased until reaching a plateau.
- Heating-up PhW: from the onset of the electric power increasing (6011 s) to the first injection of quenching water, at 7179 s.
- Quenching PhW: From the starting of pre injection water (7179 s) to the end of the experiment (after 9000 s).

The main events characterizing the experiment are summarized in Table 1. The phenomenological evolution of the experiment is detailed in (Sepold et al., 2004) and it is described in the following sections against the ASTEC results.

3. ASTEC code and model of QUENCH test-6

3.1. Description of the ASTEC code

The ASTEC code (Chatelard et al., 2016; Chatelard et al., 2014), developed by the French "Institut de Radioprotection et de Sûreté Nucléaire" (IRSN) is developed to simulate entire SA sequences in water-cooled NPPs, starting from the initiating event up to the source term evaluation. The code adopts a modular structure, with each module dedicated to simulate specific physical phenomena or reactor zones. Each module functions as an independent code and can be used either in stand-alone or coupled with other modules. The code finds wide-ranging applications, including source term evaluation, Probabilistic Safety Assessment level 2, accident management, etc. In this study, focused on reproducing early core degradation phenomena, the CESAR, and ICARE modules of ASTEC v2.2b were used.

3.1.1. CESAR module

CESAR (Chatelard et al., 2014; Gómez-García-Toraño and Laborde, 2021) is the module of ASTEC dedicated to the thermal–hydraulic simulation in the reactor coolant systems. It is a one-dimensional two-phase system code, based on a 5 or 6-equations two-phase model, and up to five non-condensable gases. In the used version of ASTEC (v2.2b), the 5-equations model was adopted. In the case of bundle or vessel quenching, a specific reflooding model is applied to better predict the progression of the quench front (Gómez-García-Toraño and Laborde, 2021). The code uses a finite volumes discretization, the time discretization applied adopts a first-order backward difference scheme, and

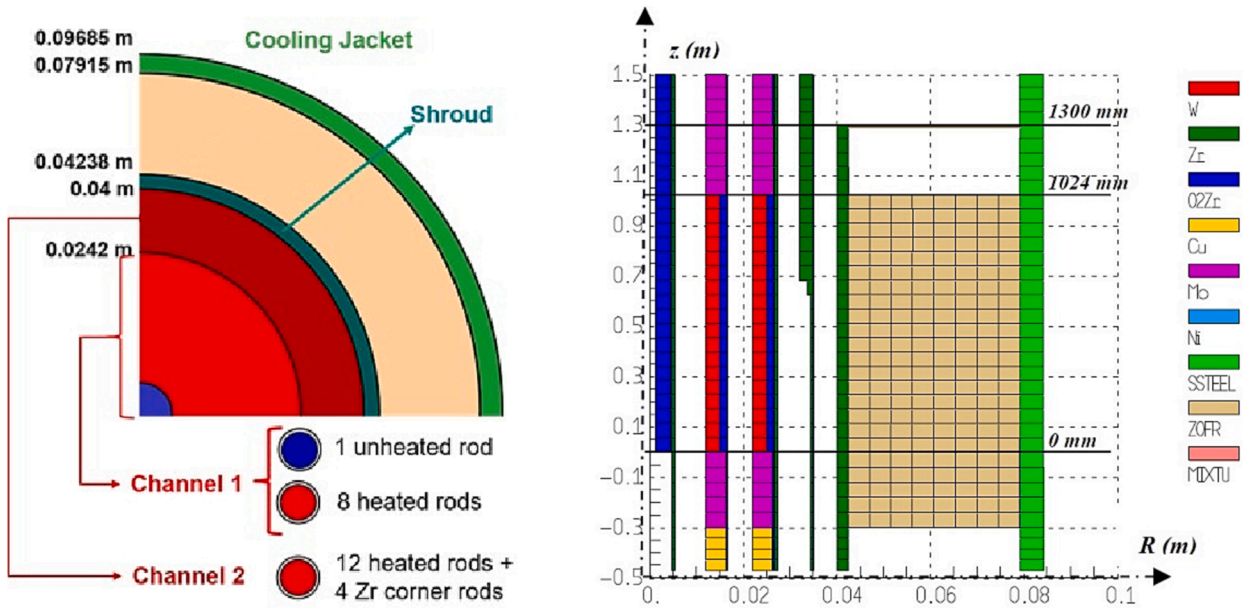

Fig. 2. Radial (left) and axial (right) nodalization of the QUENCH test-section, together with materials distribution (Gabrielli et al., 2019.).

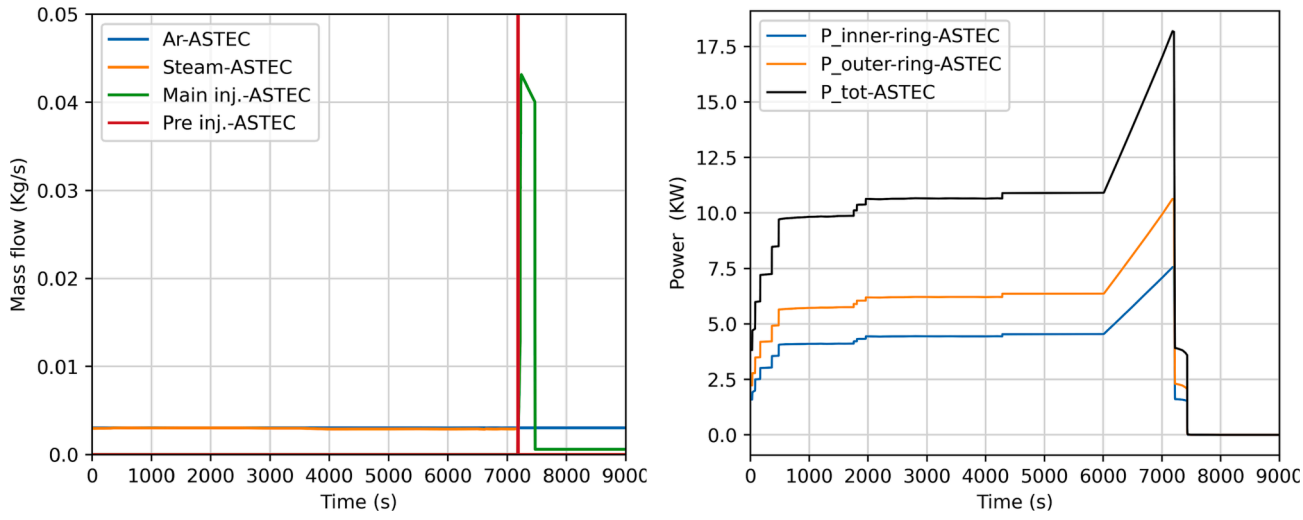

Fig. 3. Mass flow rate of fluids injections (left) and electric power generated in the heated rods (right), used as boundary conditions to the ASTEC simulation.

the system of discretized equations is solved using Newton-Raphson.

3.1.2. ICARE module

ICARE (Chatelard et al., 2014; Carénini et al., 2014) is the module dedicated to the simulation of reactor vessel and core internals by employing a 2D geometry. The core is discretized in cylindrical rings and axial meshes and a representative element can be weighted based on physical number of components. The fluid channel paths complete the meshing, allowing the 2D axial-symmetric computation of the thermal-hydraulics by CESAR. ICARE implements mechanical models, chemical reactions, fission products release models and describes core thermal behavior, degradation and relocation in the lower plenum, until the rupture of the vessel lower head.

3.2. Geometry and nodalization

The ASTEC nodalization of the experimental test section realized with ICARE module assumes azimuthal symmetry for all the elements. The thermal–hydraulic domain is radially divided in two coaxial channels in which the rods simulators are immersed. The 8 most internal rod simulators are located inside the inner fluid-channel and are collapsed into a single representative rod. The central un-heated rod is also included in the inner channel. The remaining 12 heated rods are collapsed into a single representative rod located inside the outer channel, and the same is for the 4 corner rods. The two fluid channels are surrounded by an internal shroud structure, including fiber insulation along the heated length and argon-gap along the upper unheated length. The model also includes grid spacers and plates. The annular cooling jacket tube embeds all the structures, as it is shown in the scheme of Fig. 2 - left. The model is axially divided into equal slices of 55 mm of height. Discretization and materials distribution are shown in Fig. 2 - right.

3.3. Modelling of SA physical phenomena

The relevant physical phenomena characterizing the early in-vessel degradation phase of a SA were considered in the ICARE model. In particular, the following are modelled:

- Heat transfers:
  - Conduction within each element and between the different elements in contact.
  - Convection on the elements faces facing the fluid channels (i.e. fuel rods, corner rods, grids, plates and shroud), by using the "DRACCAR" convection model (Chatelard et al., 2014; Carénini et al., 2014).
  - Radiation among fuel rod simulators, corner rods and shroud.
- Chemical interactions:
  - Oxidation of Zr components (rods cladding, corner rods, shroud, grids).
- Mechanical processes:
  - Cladding, corner rod, shroud and grids components failure occurs if the component temperature is higher than 2375 K and the ZrO_2 thickness is lower than 300 μm.
  - Cladding, corner rod, shroud and grids components failure occurs if the component temperature is higher than 2500 K.
  - Relocation of molten material along the rods and molten material oxidation has been modelled.

It should be added that Solidus and Liquids temperatures of ZrO_2 were not changed from the default values; i.e. T_{liq} = 2712 °C; T_{sol} = 2711 °C.

3.4. Initial and boundary conditions

Initial and time-dependent boundary conditions were implemented in the ASTEC model. The initial temperature distribution of the test section components (e.g. rods, shrouds, plates, grids, etc.) is given as function of the axial level. Such distributions were interpolated from the data of the available thermocouples. Also the thermodynamic quantities (mass flow rate, pressure, temperature) of the fluids injections (argon, steam and main quenching water), were derived from the recorded data and applied as time-dependent boundary condition.

It has to be mentioned that the 4 L of water pre-injection (at 370 K and 6 bar) are assumed to take place at the average rate of about 0.769 kg/s, within 5 s of injection. The mass flow rates considered are graphically reported in Fig. 3 - left. A constant pressure of 0.2 MPa is applied to the test-section top-outlet. Regarding the time-evolution of the electric power applied to the heated rods (see Fig. 3 - right), data are derived from the experimental power registered.

4. Reference ASTEC simulation of QUENCH test-6 and accuracy evaluation

The best estimate simulation the QUENCH test-6 was performed with ASTEC code V2.2 beta. In the following, the numerical results are compared against the experimental data by selecting relevant output parameters. The quantitative accuracy evaluation of the simulation is

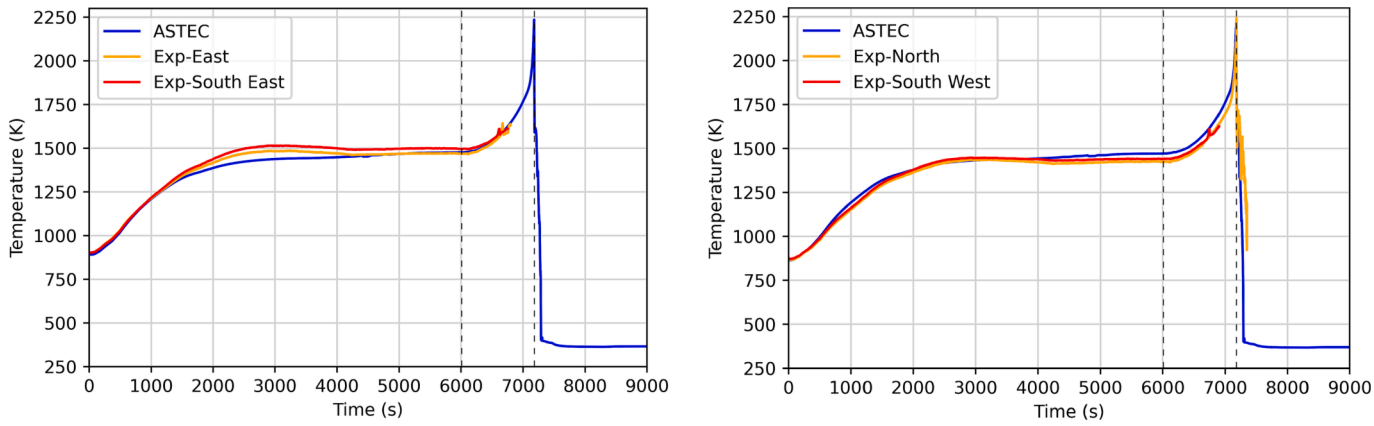

Fig. 4. Inner-ring (left) and outer-ring (right) heated rods cladding temperature, at 950 mm of elevation, from experimental data and code calculation.

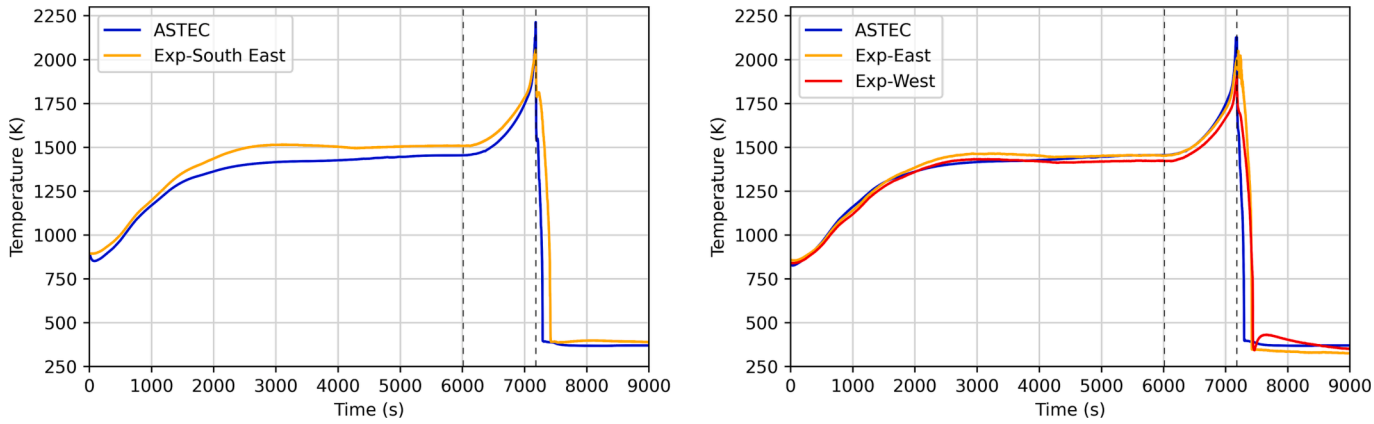

Fig. 5. Corner-rod (left) and shroud (right) temperature, at 950 mm of elevation, from experimental data and code calculation.

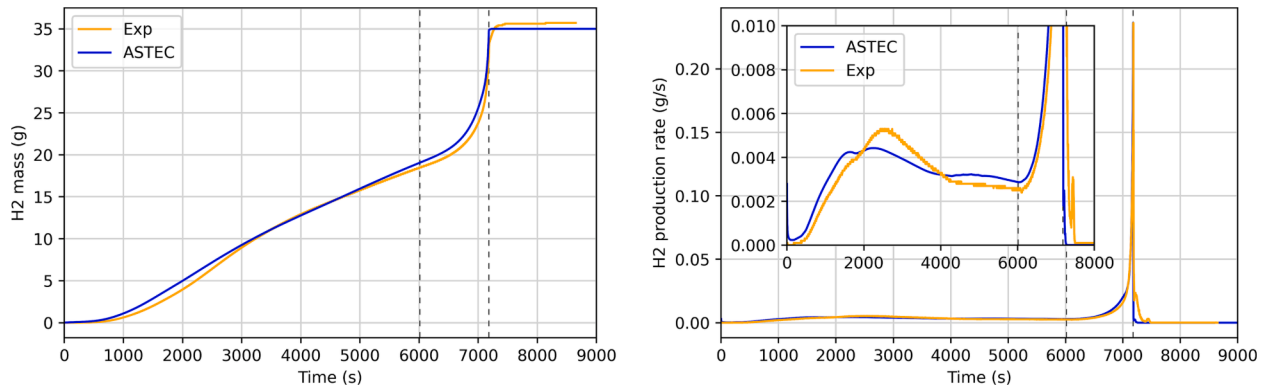

Fig. 6. H2 mass produced (left) and production rate (right) from experimental data and from code calculation.

performed by the application of the FFTBM.

4.1. Results of the ASTEC simulation against the QUENCH test-6 data

4.1.1. Pre oxidation PhW

At the onset of the test (t = 0 s), argon and steam bottom sources (around 3 g/s both) are activated in the simulation. In the ASTEC simulation, the heat power is imposed by using the experimental power as reference input data.

During the heat-up (0–2000 s), the temperature of all the structures increase, reaching the value of about 1500 K at 950 mm elevation. Quasi-steady conditions are reached in about 3000 s, and kept up to the end of the pre-oxidation PhW. The temperature evolution of corner-rod, inner and outer heated-rods, cladding and shroud, at the elevation of 950 mm (most heated level), are reported in Fig. 4 and Fig. 5. In the plots, the three PhWs are defined with vertical dashed line (at 6011 and 7179 s).

The simulated corner rod temperature, features a maximum difference of about 100 K with the experimental measurements, at the beginning of the plateau (at about 3000 s). An analogous but smaller discrepancy is shown by the temperature of the inner-ring rod (maximum of 80 K). The outer heated rods cladding and the shrouds temperatures are very close the experimental data. In the ASTEC simulation more time is needed to reach the quasi-steady conditions. Yet, the

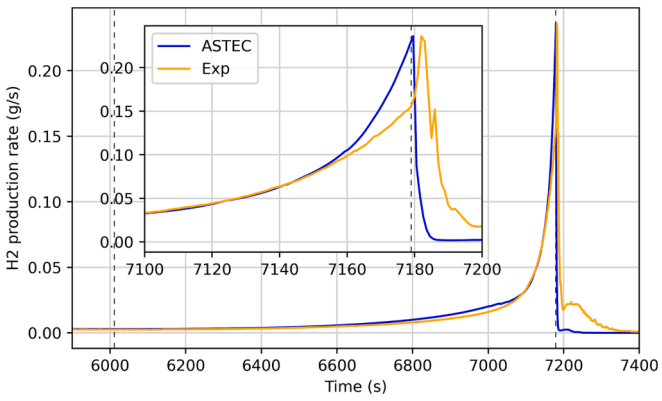

Fig. 7. H2 production rate from experimental data and from code calculation, with focus window in the heating-up PhW.

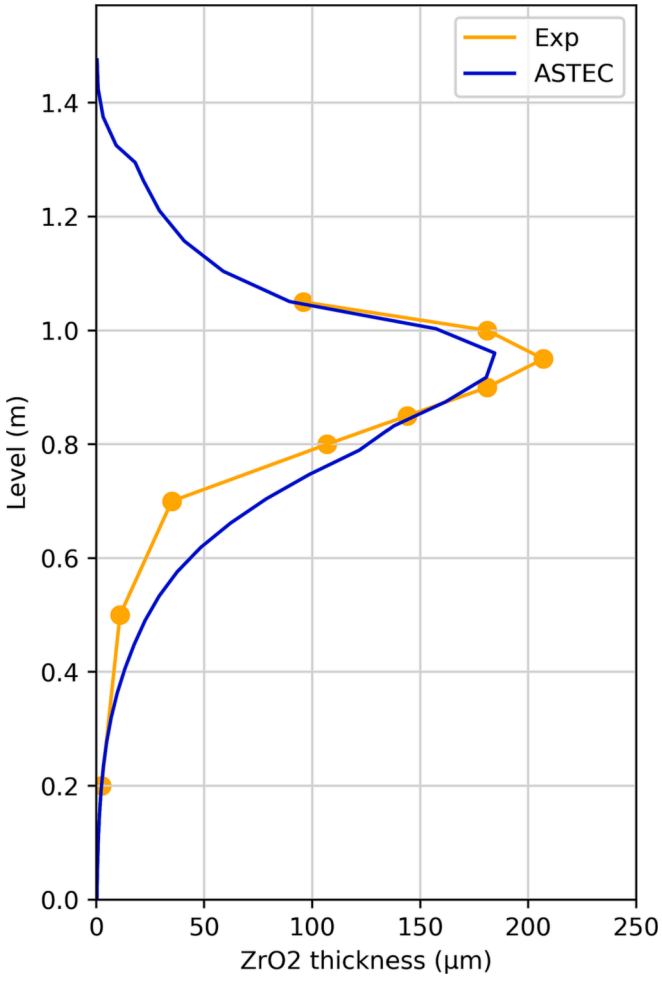

Fig. 8. Axial profile of ZrO2 thickness in the extracted corner rod and ASTEC result, at 6620 s.

temperatures evolution is in general well predicted by the code in this PhW.

Fig. 6 - left shows the total H_2 mass produced along the transient, while Fig. 6 - right reports the H_2 production rate.

The H_2 production rate follows the temperature increase during the rods heating up, showing an initial near-constant derivative. At about 2500 s, it reaches a local peak before starting to slowly decrease during the following constant-temperature phase due to the oxidation kinetics of Zr. Indeed, oxidation is governed by O_2 diffusion in the ZrO_2 layer, whose thicken increases during the oxidation process along the PhW. The ASTEC simulation shows a qualitative prediction of such phenomena. The oxidation peak occurs approximately 200 s earlier in the code and of 0.001 g/s lower. The H_2 mass produced at the end of the PhW (at 6010 s), is 18.5 g in the experiment and 19.0 g in the code simulation.

4.1.2. Heating-up PhW

At 6011 s the electric power applied to the heated rods is ramped with an increase of 0.3 W/s per rod (see Section 3.4). As can be observed in Fig. 4, some of the thermocouples failed during this phase (Sepold et al., 2004). In both the experimental and the ASTEC results, the components temperature starts to quickly increase after about 200 s from the onset of the PhW. Between the values of 1450 K and 1750 K, the rods are observed to have a temperature increase close to 0.32 K/s in both calculation results and experiment. Then, at Zr temperature of about 1770 K, the oxidation processes start to accelerate due to the high exothermic reaction heat, and a temperature escalation takes place (reaction runaway). The temperature rise is better predicted by the code in the outer-ring rods (Fig. 4 - right), where also the peak (about 2250 K) reached at 7179 s is very close to the experimental data. The corner rod and the shroud calculated temperatures (Fig. 5) feature a faster acceleration than in the experiment, ending up to final higher temperature peak.

In Fig. 7, it is reported the H_2 production rate.

It can be observed that H_2 production rate is well predicted by the code up to the onset of the oxidation acceleration (at about 7100 s). Then, in agreement with the above discussed temperature behavior, in the last 20 s of the PhW, the code predicts a higher oxidation, ending up to a higher H_2 mass. The maximum reaction-rate in ASTEC is 0.23 g/s, peaking almost at the quenching time (0.5 s later). While, from the experimental data, the maximum value, also very close to 0.23 g/s, was registered 3 s later.

It is important to point out that the experimental detection of the H_2 mass produced is expected to have up to 5 s of delay with respect to the real production (Sepold et al., 2004). The total H_2 mass at the end of the heating-up phase (7179 s), is slightly overestimated by the code (35 g against 33 g).

At 6620 s, one of the two corner-rods is extracted in the experiment in order to analyze its oxidation state. Fig. 8 shows the ZrO_2 thickness axial profile in the extracted corner-rod against the ASTEC simulation result. The same qualitative profile can be observed, with a maximum oxidation at about 950 mm level. The maximum ZrO_2 thickness is close to 200 μm in the experimental data and to 180 μm in the code. At lower elevations (between 0.2 and 0.8 m), the code predicts a few thicker oxidation layer.

4.1.3. Quenching PhW

At 7179 s, the argon source is moved to the upper part of the channels, the steam is turned off and the pre-injection water is injected at the bottom-end of the bundle for 5 s. After 26 s, the electric power is reduced from 18.2 kW to 4.0 kW, within a ramp of 16 s. At 7215 s, the main injection system starts to introduce water in the bundle. In the experiment, based on the bundle pressure behavior and on the detections of the outlet gas composition, it was deduced that the shroud and some heated rods failed at the quenching time. In the post-test direct observation, it was confirmed that a localized melting of components and limited relocation of melted mass occurred at the elevation of 950 mm (Sepold et al., 2004). Fig. 9 shows the ASTEC prediction of the bundle material compositions at the quenching time.

It can be observed the code prediction of Zr local melting in the corner-rod and in the shroud. The presence of solid ZrO_2 and ZrO layers make that the loss of integrity condition is never reached, preventing any relocation of material. In the experiment, very limited core geometry modification and mass relocation was observed. Accordingly, also a negligible internal cladding oxidation took place in the experiment. For

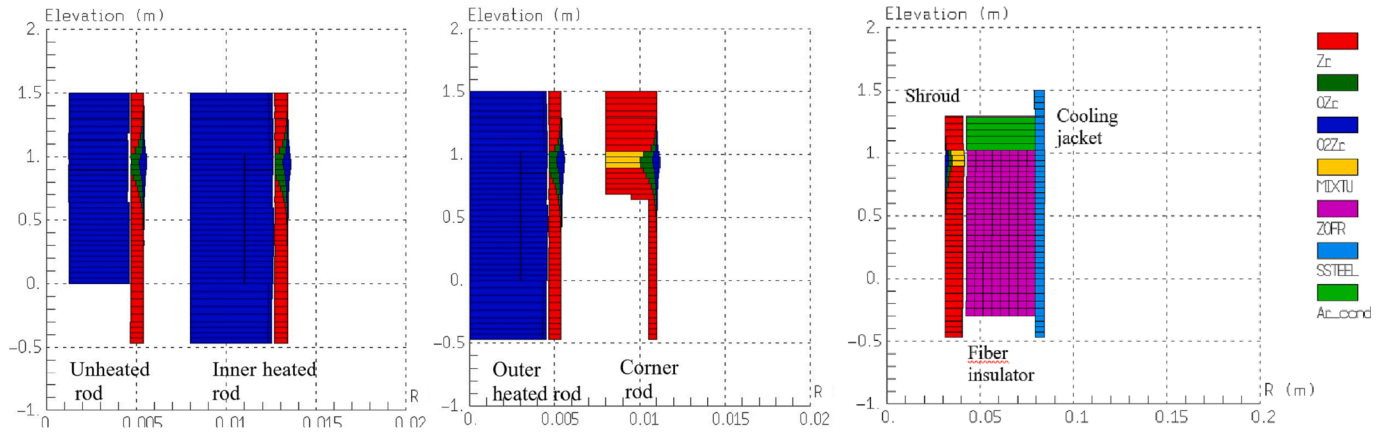

Fig. 9. Materials state of rods and shrouds components, at 7179 s in the ASTEC simulation.

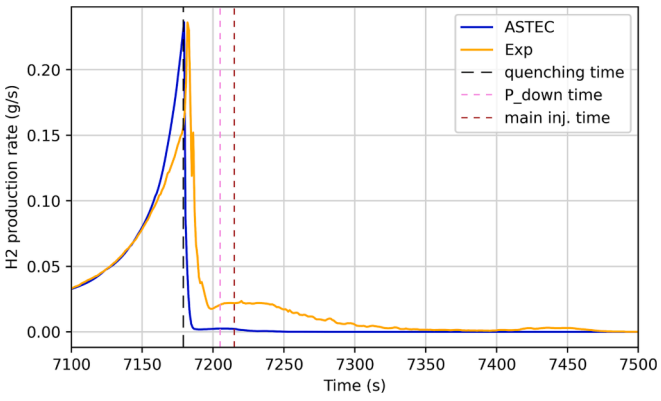

Fig. 10. H2 production rate from experimental data and from code calculation, with focus window in the quenching PhW.

this reason, by neglecting the limited relocation of melt and restricted internal oxidation, the ASTEC calculation did not result in disagreement with the experimental observations.

Regarding the temperature evolution in this PhW, for corner rods (Fig. 5 - left) and heated rods (Fig. 4), a qualitative agreement can be observed: a first fast temperatures drop of several hundred degrees in about 15 s takes place after the pre-injection. It is followed by a slight increase of the cladding temperature between the end of the pre-injection and the onset of the main injection. The second cooling, due to the main cooling water injection, features a moderate temperature decrease, ending up to the saturation temperature.

In Fig. 10 it is reported the H_2 production rate with a focus on the present PhW.

It can be observed that the code predicts a rapid oxidation decrease after the onset of quenching, reaching almost the zero H_2 production in few seconds. Considering a delay of 5 s for the experimental detection, it is very close to the calculated result. Yet, in agreement with the temperatures behavior, the experimental data of H_2 production does not

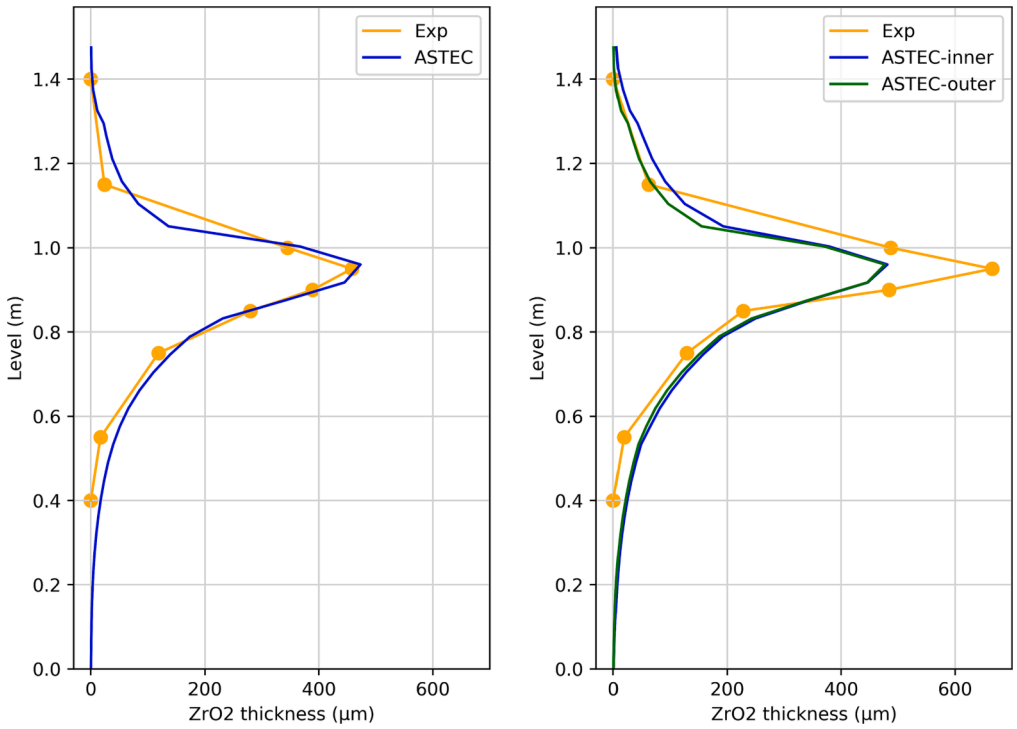

Fig. 11. Axial profile of ZrO2 thickness averaged in the corner rods cladding (left) and in the heated rods cladding (right) against ASTEC results, at calculation end (9000 s).

Table 2
FFTBM analysis results.

Variables	Pre-oxidation PhW		Heating up PhW		Quenching PhW	
	AA	WF	AA	WF	AA	WF
M_H2_g	0.04	0.04	0.11	0.06	0.15	0.07
W_Lev_1	0.13	0.10	0.06	0.11	0.61	0.12
W_Lev_2	0.13	0.10	0.06	0.11	0.59	0.12
T_CRod	0.07	0.03	0.14	0.07	0.41	0.02
T_HR_inner_1	0.03	0.02	*	*	*	*
T_HR_inner_2	0.04	0.02	*	*	*	*
T_HR_outer_1	0.05	0.04	0.05	0.06	*	*
T_HR_outer_2	0.04	0.04	*	*	*	*
T_Shro_1	0.04	0.03	0.18	0.06	0.40	0.02
T_Shro_2	0.04	0.02	0.10	0.07	0.46	0.03
Total	**0.06**		**0.10**		**0.44**	

* failed thermocouples.

stop completely, but reaches an average value of 0.02 g/s, which is kept for around 140 s. The total amount of H_2 produced in the simulation is higher of only around 1 g (Fig. 6).

Fig. 11 shows the axial profiles of ZrO_2 thickness in the corner rods (left) and in the heated rods (right) at the end of the test (9000 s). The experimental profile is calculated by averaging the ZrO_2 thickness in all the rods of the same type (heated and corner rods). Regarding the code, the thickness in the representative rods is reported in Fig. 11.

The comparison in the corner-rods features in agreement from both the qualitative and the quantitative point of view. The two simulated heated-rods profiles underestimate the Zr oxidation at 950 mm elevation, but the code predicts the qualitative oxidation profile. The oxidation thickness in the experiment at 950 mm is about 680 μm, while the calculated one at the same elevation is 200 μm lower.

4.2. Application of FFTBM for quantitative accuracy evaluation

4.2.1. The FFTBM method

The quantitative accuracy of the simulation results, with respect to the experimental data, can be evaluated by the application of the Fast Fourier Transform Based Method (FFTBM; Ambrosini, 1990; Bersano et al., 2020). In this methodology, the difference between calculated and experimental data is passed from the time domain to the frequency one using the Fast Fourier Transform. In this way, the evaluation accuracy is based on two parameters: Average Amplitude (AA) and Weighted Frequency (WF; Prošek et al., 2008; Prošek et al., 2015). AA is the main parameter for the accuracy evaluation: the lower is its value and the more accurate is the result. Whereas, WF can be considered an additional qualitative data (Ambrosini, 1990), providing information about the frequencies that more contribute to discrepancies. The JSI FFTBM Add-In 2007 was used to apply the FFTBM. The tool is developed at Jožef Stefan Institute (Slovenia; Prošek et al., 2008; Prošek et al., 2015; Prošek, 2007). The default cut-off frequency of 0.4 Hz was used.

Usually, several output parameters are considered and the total AA is computed adopting weighting factors According to the authors knowledge, the selection of weighting factors may be subjective and require experiments to be set up (Prošek et al., 2002). Since no widely recognized factors have been yet derived for specific SA quantities (e.g. H_2 mass production), the factors were set equal to one and the total AA is reduced to the average AA of the various parameters (as it was done in (Prošek et al., 2005).

Ten parameters were considered for the evaluation: H_2 mass produced, a water collapsed level for each channel and seven wall temperatures at different locations. The reference threshold values for the AA for the accuracy evaluation are (D'Auria et al., 1999):

- AA $\leq$ 0.3: very good code prediction;
- 0.3 < AA $\leq$ 0.5: good code prediction;
- 0.5 < AA $\leq$ 0.7: poor code prediction;
- AA $\geq$ 0.7: very poor code prediction.

4.2.2. Results of the FFTBM study

Table 2 summarizes the FFTBM results. The data of thermocouples failing during the PhW were excluded from the evaluation and are highlighted with a "*". In the pre-oxidation PhW, the total AA is 0.06 and the code prediction can be classified as very good for all the considered parameters. In the heat up PhW the prediction of all parameters is classified as very good (except failing thermocouples), with a total AA of 0.10. Finally, in the quenching PhW the code prediction for the remaining temperature measurements can be classified as good, due to the general anticipation of the temperatures drop. The water levels AA are slightly higher than 0.5 due to a slight underestimation of experimental data.[1] The prediction of the H_2 production is classified as very good (AA of 0.15). The total AA is equal to 0.44 in this last PhW.

5. Uncertainty quantification

The present section deals with the UQ analysis of the ASTEC simulation. The methodology used and the set-up of the study are first described. Following, the results of the UQ analysis are reported and discussed.

5.1. Methodology of uncertainty and sensitivity analysis

5.1.1. Description of the UQ methodology

UQ of deterministic code results can be carried out through the application of a specific methodology. The one selected in the present work is the *probabilistic propagation of input uncertainties* (D'Auria et al., 2008; Bersano et al., 2020; Glaeser, 2008). This method is based on the selection of input uncertain parameters, defined by a reference value (best-estimate value), a range of variation and a Probability Density Function (PDF) type. A random sampling (e.g. Monte Carlo) of the input uncertain parameters is performed, in order to obtain a sets of values that will be used as input of several code calculations of the same sequence. All the uncertain input parameters assume different values in each performed simulation. A key point in this process is the choice of the number of calculations (sampling size). This is selected on the base of the Wilks confidence interval formula (Glaeser, 2008; Wilks, 1941; Wilks, 1942), that provides a minimum sampling size based on the chosen values of *probability content* and of *confidence level*. An advantage of the method is that the number of calculations needed is not influenced by the number of input uncertain parameters (Guba et al., 2003).

In addition, the obtained code results can be subjected to sensitivity analysis aimed at characterizing the importance of each input uncertain parameter in the propagation of the uncertainty to each output FOM. This analysis is carried out through the calculation of correlation or sensitivity coefficients, and those used in the present study are Pearson and Spearman correlation coefficients, respectively characterizing the linear and the monotonic correlation between an input parameter and a FOM. In addition, LASSO regression coefficients were also calculated to validate the obtained correlations (Goodfellow et al., 2016). Absolute

[1] In relation to the FFTBM, it has to be underlined that the presence of oscillations in the experimental and/or calculated data could give relatively high values of AA even if the curves seem in reasonable agreement. These oscillations in fact can introduce higher frequencies that in principle could be not physical but add spurious contribution in the AA computation increasing its value. Therefore, in a validation process for safety review purpose, more detailed analysis could be necessary to analyze the nature of the oscillations and by investigating the AA values as a function of the cut-off frequency. Within this regards it is also important to underline the role of the weight of each parameter for the calculation of the total accuracy in the FFTBM; this weight, in fact, determines the contribution of each parameter for the computation of the total accuracy.

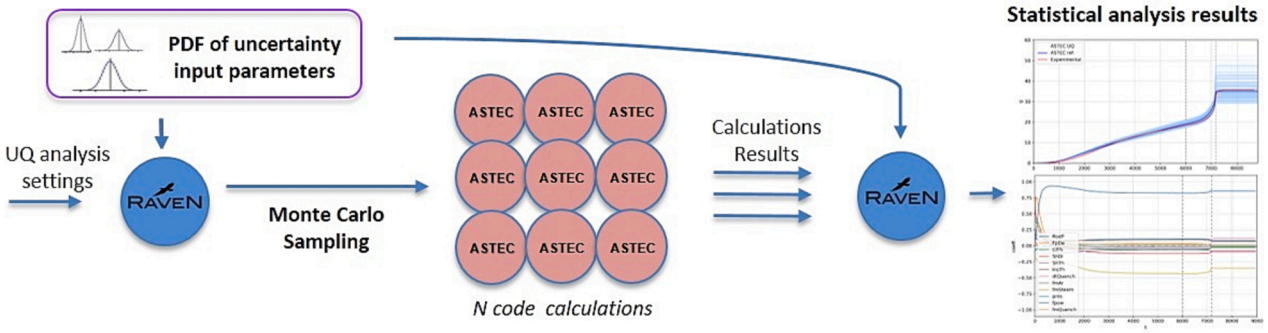

Fig. 12. Scheme of ASTEC – RAVEN coupling workflow for UQ analysis (Maccari, 2021).

values of the coefficient higher than 0.5 classifies the correlation as *significant*; between 0.2 and 0.5 it is assumed *moderate*; and below 0.2 it is considered *low or absent* (Bersano et al., 2020). It should be mentioned that despite the number of input uncertain parameters does not affect the number of required calculations (according to Wilks), it is also important to consider that to guarantee reliable sensitivity measures the sampling size should be much larger than the number of input uncertain parameters (Perez et al., 2011).

5.1.2. Description of RAVEN

RAVEN (Alfonsi et al., 2020; Risk Analysis and Virtual ENvironment), developed by Idaho National Laboratory (INL), is the uncertainty tool employed in the current work. It is developed in Python (Rossum, 1995) as an open-source code, using an object-oriented approach. Parallel simulations, for both standard and High Performance Computing (HPC) systems, are fully supported. RAVEN software includes tools, models and algorithms for parametric and probabilistic analysis and it is designed to perform: classical and advanced statistical analyses, parametric studies, limit surfaces determination, machine learning with artificial intelligence algorithms, etc.

5.1.3. RAVEN – ASTEC coupling for UQ application

RAVEN disposes of specific interfaces to exchange information with many codes (e.g. MAAP, MELCOR, RELAP). For other codes, the coupling can be done through a generic interface or, as an alternative, users can develop their own specific Python interface to be included in the source-code. By choosing this last option, a dedicated RAVEN-ASTEC coupling interface was developed by ENEA (Maccari et al., 2021). The ASTEC input-deck was also properly modified for the codes coupling, i.e. to allow RAVEN to retrieve the information needed to modify the input-parameters. The main settings to the UQ analysis were included in the XML file inputted to RAVEN, along with information needed to run the calculations on a multicore HPC platform. In this way, RAVEN is able to drive the process needed for the UQ study, i.e.:

- It samples the values of the selected input uncertain parameters;
- Creates a set of N different input-decks of the same sequence by using the sampled values;
- Launches the code simulations communicating with the computer infrastructure;
- Collects the simulations results and create summary results CSV files.

The ASTEC-RAVEN coupling workflow for UQ analysis is summarized in Fig. 12. Despite RAVEN disposes of own statistical, in this case the post-processing of the calculations output data and the assessment of the sensitivity analysis were realized by using home-made scrips developed with Python statistics libraries (Rossum, 1995).

5.1.4. Definition of uncertain input parameters

23 input uncertain parameters were selected by KIT. These include

Table 3
Uncertain parameters of type: geometry of the bundle; initial and boundary conditions.

#	Parameter	Reference value and range	PDF type	Short name
1	Rod pitch (mm)	14.3 ± 0.15	Uniform	RodP
2	External diameter of fuel pellet simulator (ZrO_2) (mm)	9.15 ± 0.02	Uniform	FpDe
3	Thickness of Cladding (mm)	0.725 ± 0.00725	Uniform	ClTh
4	Internal diameter of Shroud (mm)	80 ± 0.8	Uniform	ShDi
5	Thickness of Shroud (mm)	2.38 ± 0.023	Uniform	ShTh
6	Thickness of Insulator (mm)	37.0 ± 0.37	Uniform	InsTh
7	Instant of main quench water injection (s)	7215 ± 0.5%	Uniform	dtQuench
8	Mass flow rate of quench water (kg/s)	*f(t)* experimental value ± 0.5%	Normal	fmQuench
9	Mass flow rate of Argon (kg/s)	*f(t)* experimental value ± 2%	Normal	fmAr
10	Mass flow rate of Steam (kg/s)	*f(t)* experimental value ± 2%	Normal	fmSteam
11	Pressure at the bundle outlet (bar)	2.0 ± 2%	Normal	pres
12	Electrical power (kW)	*f(t)* experimental value ± 2%	Normal	fpow
13	Temperature of quenching water (K)	*f(t)* experimental value ± 2%	Normal	fTquench
14	Fuel/Clad internal pressure (bar)	2.2 ± 2%	Normal	pGap

Table 4
Uncertain parameters of type: integrity criteria of cladding; radiative H.T.; convection H.T.; material relocation parameters.

#	Parameter	Reference value and Range	PDF type	Short name
15	Threshold thickness (μm)	300 ± 10%	Uniform	ThkFail
16	Failure temperature of the ZrO_2 layer (K)	2374 ± 5%	Uniform	TempFail
17	Rod anisotropic factor	0.5 ± 10%	Uniform	HeatRani
18	Shroud anisotropic factor	0.15 ± 10%	Uniform	HeatSani
19	Heat transfer coefficient due to droplet projection	100 ± 5%	Uniform	DropHd
20	Height above the quench front concerned by droplet projection	0.8 ± 5%	Uniform	DropZd
21	Threshold void fraction to allow exchange with liquid droplets	0.999; [0.99, 0.999]	Uniform	DropThr
22	Maximum value of the ratio permeability/viscosity	0.1 ± 5%	Uniform	MovKsmx
23	Minimum liquid fraction allowing the material relocation (%)	0.0; [0.0, 5.0]	Uniform	MovLiq

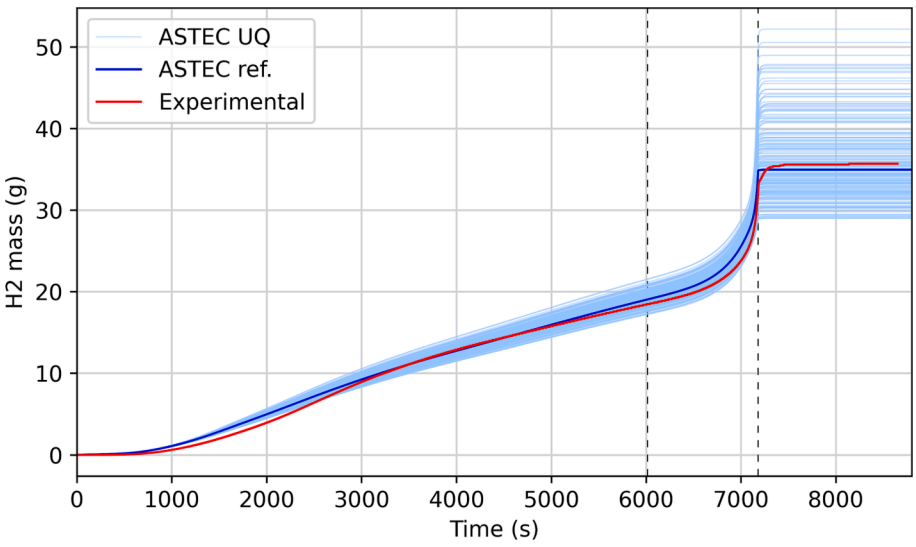

Fig. 13. Dispersion band of H2 cumulative mass, against experimental and reference values.

geometric data parameters, initial and boundary conditions, integrity criteria and heat transfer models parameters. Reference value, range of variation and PDF types have also been provided by KIT in the framework of the CRP-I31033 (https://www.iaea.org/projects/crp/i31033), as a result of a study from public references, parametric studies and expert judgment. Table 3 and Table 4 summarize the input uncertain parameters used in the analysis with the associated ranges and PDFs.

5.1.5. Definition of FOMs and sampling size

The FOMs selected for the UQ analysis, among the ones proposed by KIT, are:

- Cumulative H_2 mass produced (kg);
- Internal temperature of central rod simulator, at 950 mm of elevation (K);
- H_2 production rate (kg/s);
- Profile of ZrO_2 in the corner rod, at 6620 s (μm);
- Profile of ZrO_2 in internal-ring heated-rod, at calculation end (μm).

The UQ analysis of the ASTEC simulation was developed through the application of the probabilistic propagation of input uncertainties, following the methodology described in this Section. The number of code runs was defined based on Wilks (Wilks, 1941; Wilks, 1942; Guba et al., 2003; Wald, 1943), by considering the one-sided tolerance limit on 5 FOMs. Hence, by imposing a required probability content and a confidence level of 95%, a minimum number of 181 calculations is obtained. Therefore, accounting for possible code failures, the total number of simulations was raised to 200.

5.2. Results of UQ analysis

All the 200 ASTEC runs were completed without any failure. The first FOM analyzed is the H_2 cumulative mass, representing also a measure of the overall Zr oxidation. Fig. 13 reports the results dispersion band, (obtained by plotting the results of all the ASTEC calculations) against the experimental data and the reference calculation.

In the figure, a near constant increase of the band-width during the pre-oxidation PhW can be observed. After around 2200 s, the experimental data is included in the dispersion band and very close to the reference result, proving the good quality of the code prediction in this phase.

The heat-up PhW is characterized by a moderate increase in the

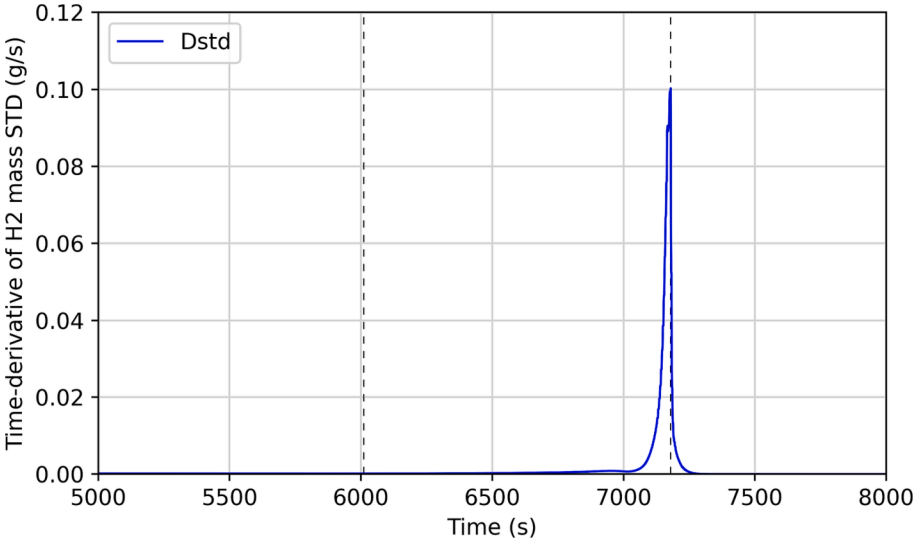

Fig. 14. Time-derivative of STD of cumulative H2 mass in ASTEC result.

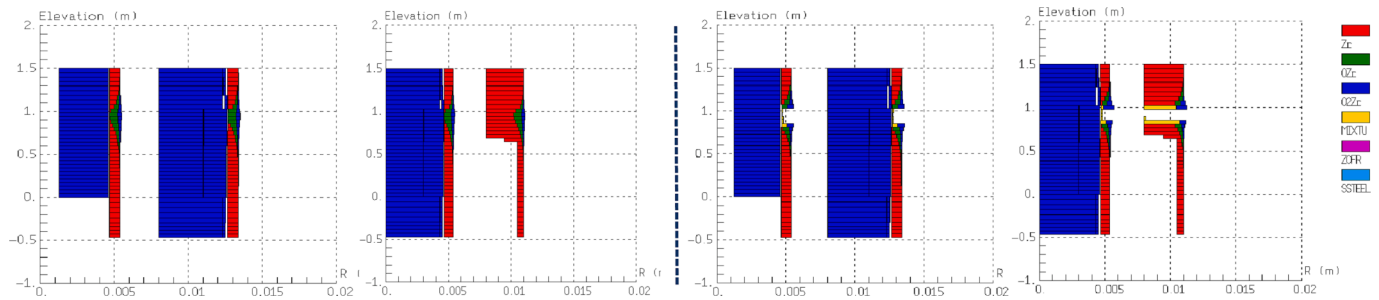

Fig. 15. Materials state of rods components, at 7179 s of ASTEC simulation, for lowest oxidation result (left) and highest oxidation result (right).

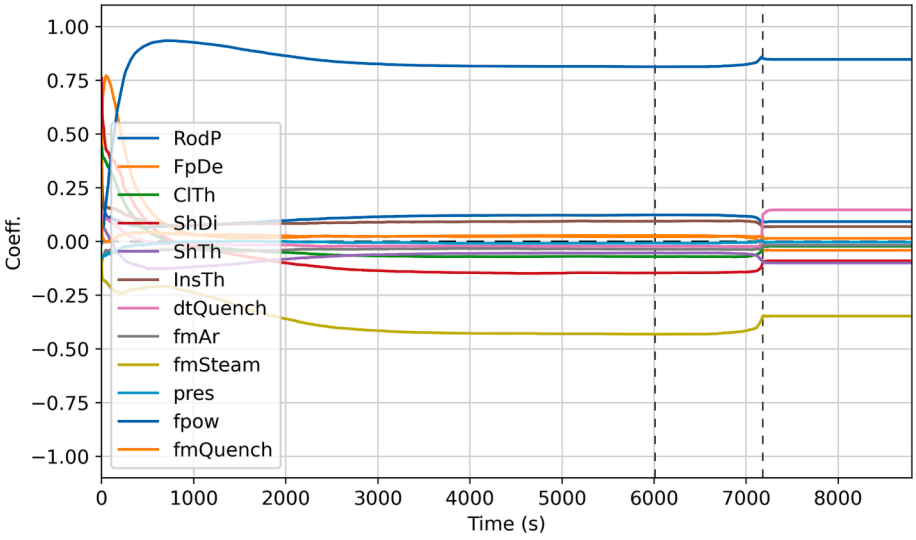

Fig. 16. Spearman correlation coefficient related to cumulative H2 (geometric and boundary conditions input parameters).

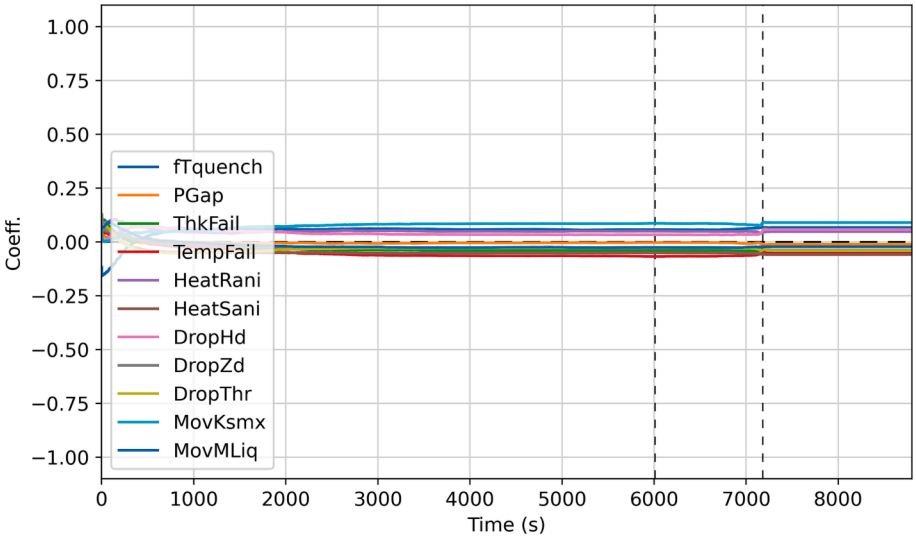

Fig. 17. Spearman correlation coefficient related to cumulative H2 (cladding integrity criteria and physical models).

dispersion of the H_2 cumulative mass, until 7050 s of simulation. At this point (onset of oxidation acceleration), the dispersion of the results (band-width) start a very fast increase. To better asses this behavior, the time-derivative of the Standard Deviation (STD) of this FOM is plotted in Fig. 14 between 5000 and 8000 s. This can be defined by:

$\frac{d}{dt}[STD(M_{H2}(t))]$; with STD being the Standard Deviation operator, and $M_{H2}(t)$ being the cumulative H_2 mass FOM.

The evolution of STD derivative highlights the fast spread of results taking place from around 7050 s and rapidly reducing around 50 s after the onset of quenching (at around 7230 s). The results dispersion band presents a width of 23 g at the end of the transient.

Additional important observations can be drawn by looking at Fig. 15, showing the rods material composition at quenching time, for 2 simulations of the 200, picked up at the two extremes of the H_2 results

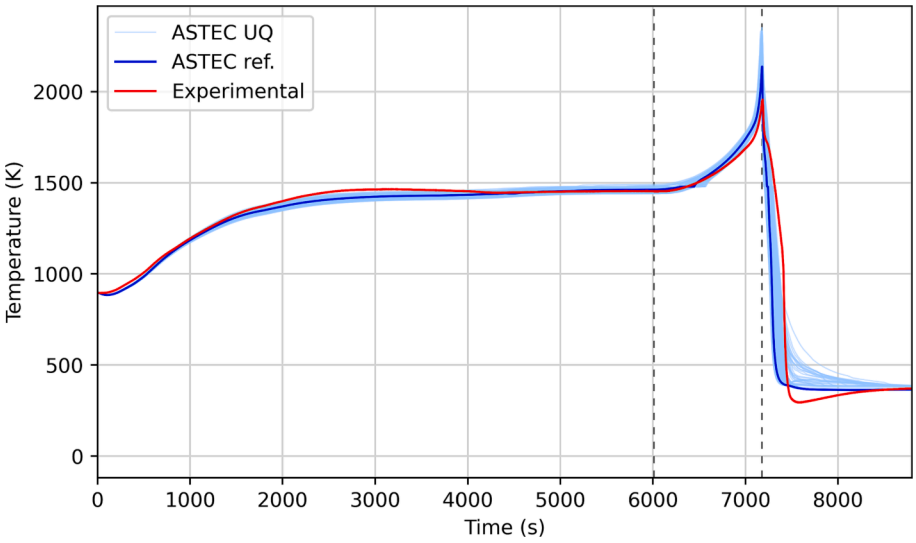

Fig. 18. Dispersion band of central rod internal temperature, against experimental and reference values.

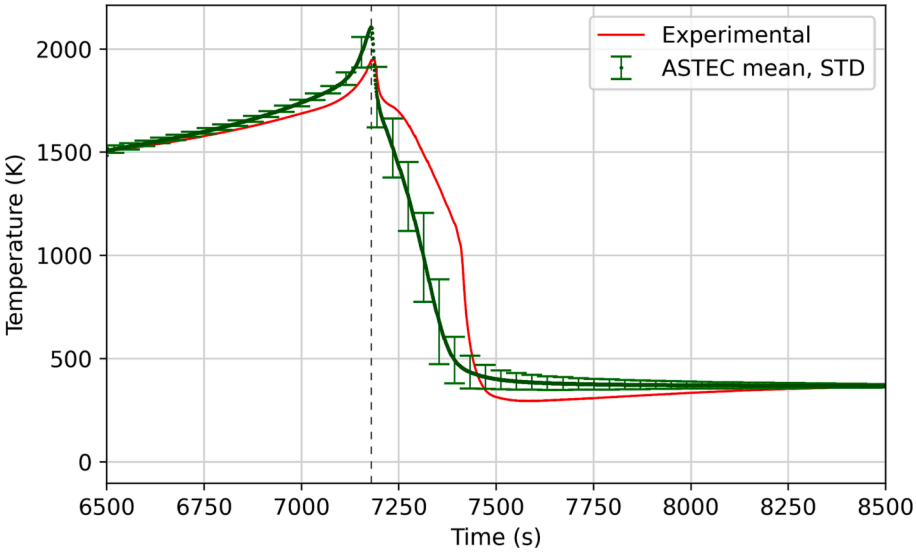

Fig. 19. Mean value and STD of central rod internal temperature, against experimental data.

dispersion band (lowest oxidation case on the left and highest oxidation case on the right).

The scenario on Fig. 15 - left features no melting of materials; while the one on the right is characterized by localized melting and relocation nearby the region of 950 mm elevation. The phenomenology observed in the reference scenario (localized melting without relocation) in Fig. 9, can be considered to be in between the two, as well as the phenomenology observed in the experimental test (see Section 4.1.2).

Regarding the correlation and sensitivity analysis, the time-dependent values of the Spearman correlation coefficients related to the H_2 cumulative production were computed for the 23 uncertain parameters and plotted in Fig. 16 and Fig. 17. Since the other computed coefficients (i.e. Pearson and LASSO Regression) were in agreement with the Spearman one, for the sake of brevity these have not been reported.

It can be evinced that only two uncertain parameters show a moderate or significant correlation with the FOM along most of the sequence (after 1000 s): *steam mass flow rate* (moderate negative correlation) and *power in the bundle* (significant positive correlation).

The second FOM considered is the internal temperature of the central (unheated) rod simulator, at the elevation of 950 mm. Fig. 18 reports its dispersion band and reference value against the experimental data.

In this case, the spread of results is in general lower than for the previous FOM and it can be observed that the spread of results behaves differently: a first minor uncertainty increase during the heat-up of the bundle can be observed for the present FOM, whereas, a major increasing takes place after the onset of quenching, with its maximum value reached at around 7350 s during the cooling of the bundle. A better highlight of this point can be assessed by plotting mean value and STD of the FOM between 6500 s and 8500 s in Fig. 19.

Fig. 19 this figure also underlines as the experimental value is not included in the dispersion band (and in the STD) during the temperature decreasing.

The Spearman correlation coefficients for the same FOM are reported in Fig. 20 and Fig. 21.

As in the previous case, during pre-oxidation and heat-up PhWs, the main correlations are observed with the *power in the bundle*, and the *steam mass flow rate*. Yet, after the onset of quenching quite different correlations are captured: the majors are observed with the *instant of quenching injection* (significant-positive), and the *threshold void fraction to allow exchange with liquid droplets* (significant-negative).

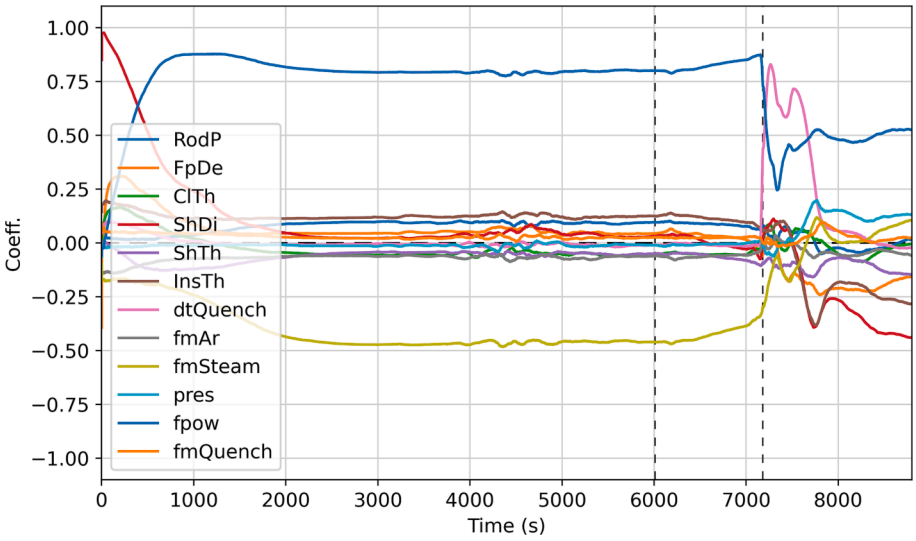

Fig. 20. Spearman correlation coefficient related to internal temperature of the central rod (geometric and boundary conditions input parameters).

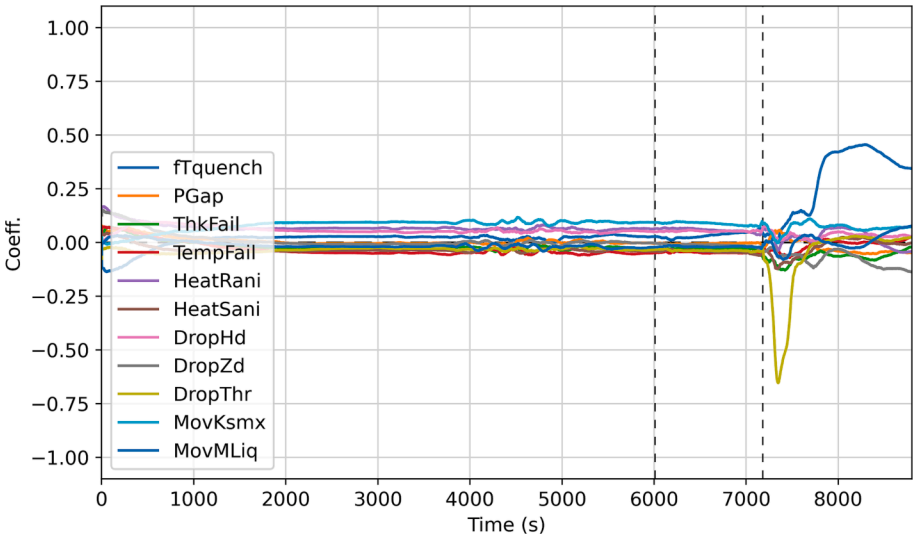

Fig. 21. Spearman correlation coefficient related to internal temperature of the central rod (cladding integrity criteria and physical models).

The results dispersion of the third FOM, i.e. the H_2 production rate, is shown in Fig. 22, highlighting the last part of heat-up and quenching.

It can be observed that the dispersion band-width is very thin during the first PhW, while it increases considerably after the acceleration of the oxidation (at about 7050 s). After quenching, the width of the dispersion band rapidly reduces again. It is important to underline that the experimental data is always enclosed in the dispersion band, except for the 150 s after quenching.

The sensitivity and correlation analysis on this FOM results in correlations very similar to those obtained for the internal temperature of the central rod, in Fig. 20 and Fig. 21, and their plot are not reported for the sake of brevity.

The results dispersion band of the two remaining FOMs (ZrO_2 profile in the corner rod at 6620 s and ZrO_2 profile in internal-ring heated-rod at calculation) is reported in Fig. 23.

In Fig. 23 - left the results dispersion is in general moderate and the maximum width of 55 μm is reached at the level of 950 mm. In Fig. 23 - right, at the most oxidized elevations (800–1150 mm) it is observed a higher spread of results. Indeed, in some of the simulations it is predicted a local cladding failure and relocation of material (Fig. 15), in this case the ZrO_2 thickness is reported with the value of 0 in the figure. Such situation can be considered as a bifurcation of the output domain of this FOM due to the cliff-edge effect of the core degradation phenomenology.

In Fig. 24 and Fig. 25 are reported the related Spearman coefficients.

From Fig. 24, it can be inferred that the *electrical power in the bundle* parameter has a significant positive correlation at all the elevations, *steam flow rate* has a moderate negative correlation at elevation lower than 1300 mm, and *shroud internal diameter* features a moderate negative correlation only at elevations presenting a minor oxidation (above 1300 mm and below 500 mm).

Also the coefficients in Fig. 25 show the same correlations, with the difference that the correlation with *shroud internal diameter* is positive at the bottom and negative at the top.

6. Discussion and conclusions

6.1. Adopted methodology

The presented study proves the effectiveness of the adopted methodology consisting of accuracy evaluation and UQ in the assessment of the code capability to simulate the main involved SA phenomena in an experimental transient.

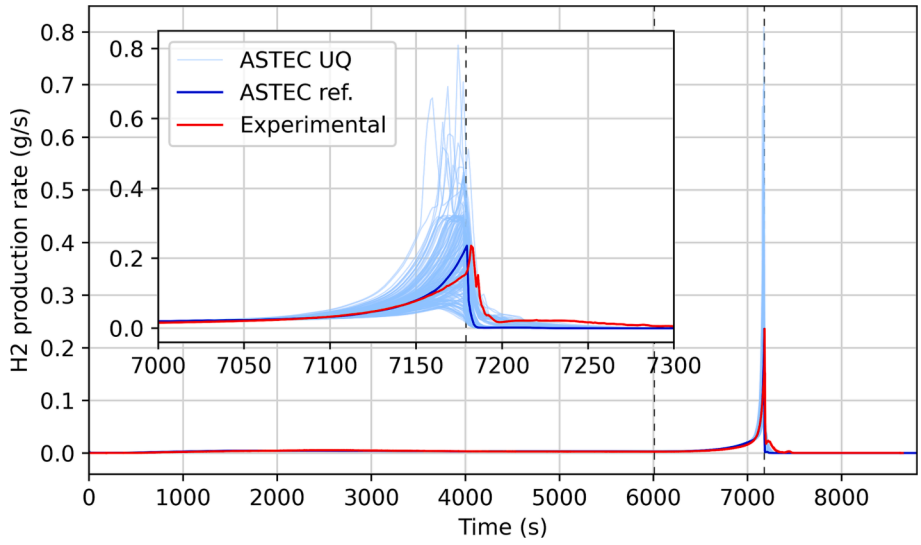

Fig. 22. Dispersion band of H2 production rate, against experimental and reference values.

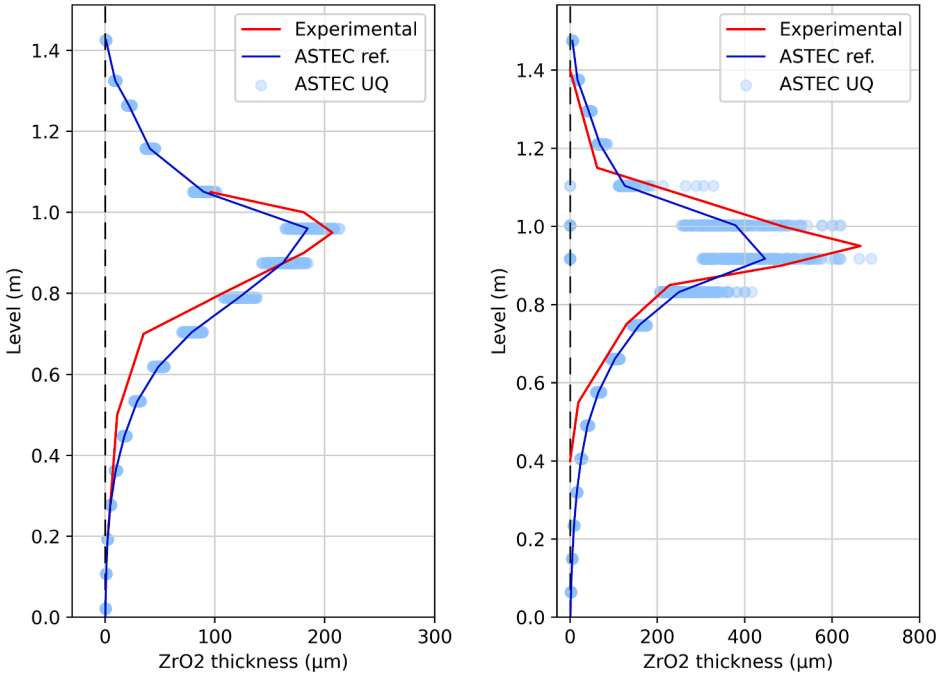

Fig. 23. Dispersion band of ZrO2 profile in the corner rod at 6620 s (left) and of ZrO2 profile in internal-ring heated-rod at calculation end, against experimental and reference values.

Indeed, the comparison of the reference (best-estimate) simulation with the experimental data is crucial to identify the physical phenomena governing the sequence and to evaluate the code qualitative prediction for each of them. The accuracy of the code is then quantitatively evaluated using the FFTBM method. Finally, the UQ analysis provides information regarding the uncertainty affecting the code predictions. The probabilistic propagation of input uncertainty method, based on Wilks, is advantageous in cases where a large number of input uncertain parameters are involved, as this number does not influence the sampling size. In addition, the correlation and sensitivity analysis identifies the main sources of uncertainty, which can be reduced with R&D efforts in further studies.

6.2. *Reference calculation and accuracy evaluation*

From the visual comparison and the FFTBM results, it is concluded that ASTEC features a very good quantitative prediction of the phenomena governing the pre-oxidation PhW (i.e. heat exchange and oxidation kinetics of Zr in super-heated steam-Ar environment). Also, during the heating-up PhW, the prediction was classified as very good, and sole discrepancy lies in the prediction of a faster heating of some components (e.g. corner rod, shroud). The quenching PhW features some discrepancies, but the general accuracy was evaluated as good. In particular, the quenching leads to a faster temperatures drop and a following earlier stop of the oxidation in the calculation. This could be attributed to a slight overestimation of convection heat exchange by the code during quenching and by the modelling assumptions adopted. For a deeper understanding of the underlying cause, further investigations are

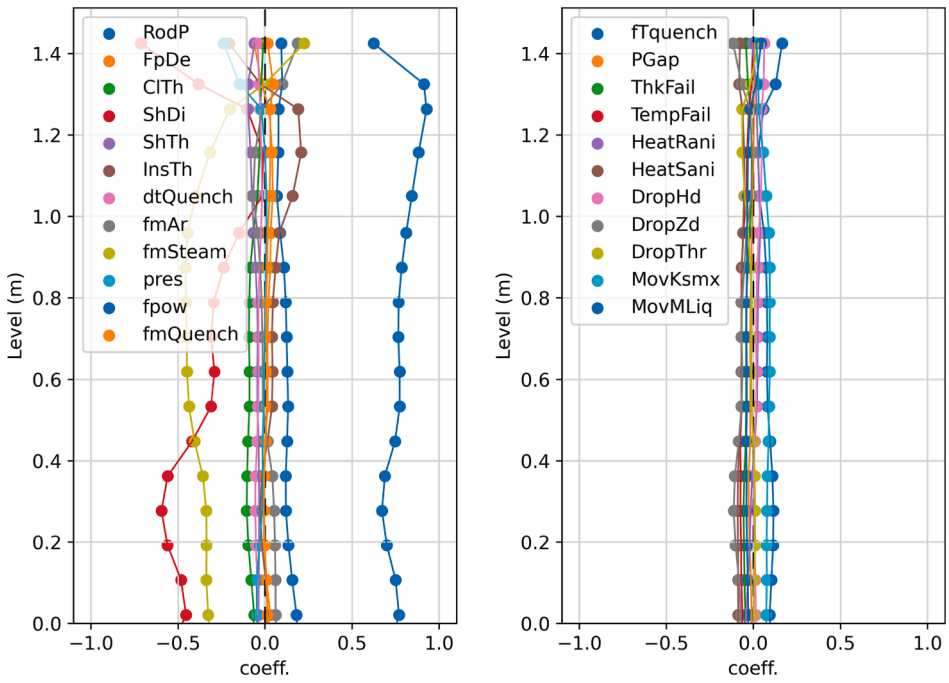

Fig. 24. Spearman coefficient related to corner rod ZrO2 thickness at 6620 s, for geometric and boundary conditions (left), and for cladding integrity criteria and physical models (right).

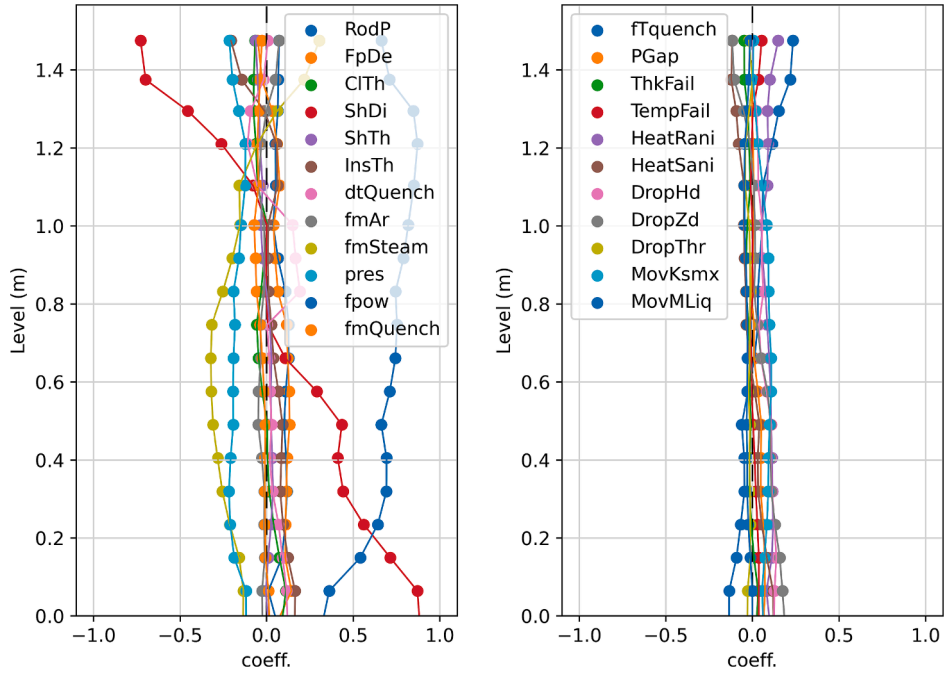

Fig. 25. Spearman coefficient related to ZrO2 thickness in inner-ring hated rods at calculation end, for geometric and boundary conditions (left), and for cladding integrity criteria and physical models (right).

required on this matter.

From a phenomenological point of view, ASTEC capture a local melting of materials at the most heated-up level without a loss of the integrity conditions, similarly to what is observed in the post-experiment observation (local material melting occurs without loss of structure integrity). Altogether, the code prediction of the total H_2 produced is only 1 g lower than the experimental one.

6.3. *Uncertainty analysis*

The UQ analysis allowed to characterize the uncertainty of the simulation in terms of width of the results dispersion band of each FOM. Regarding the cumulative H_2 production, it features a fast increase of uncertainty during the oxidation acceleration. This behaviour should be explained by the non-linear evolution of the oxidation reaction at temperatures above about 1770 K (reaction runaway). The dispersion bands of ZrO_2 thickness profile confirms this finding. A different behaviour is

observed for the central rod temperature at 950 mm level: the spread of results dispersion in this case takes place mainly during quenching.

A key outcome is that a reason for the general results dispersion spread should be attributed to a phenomenology bifurcation, deriving from the fact that the reference case (in agreement with the experiment) is on the edge of changing in a core-degradation phenomenon. Indeed, the conditions for loss of integrity and relocation are very close to be reached in rods cladding and shroud. As a consequence, due to the perturbation inserted by the uncertain parameters sampling, some of the UQ simulations end up to a different phenomenology, i.e. to structures failure and material relocation. Furthermore, this also determines additional oxidation and H_2 production since the cladding internal surfaces get available for oxidation, hence increasing the results spread. In general, SA phenomenology and codes models are characterized by non-linear (e.g. oxidation runaway, etc.) and cliff-edge effect (e.g. failures and relocations) behaviours. Such feature can be considered a key element potentially increasing the uncertainty of SA code simulations.

6.4. Correlation and sensitivity analysis

With the aim of finding the main sources of uncertainty a time-dependent correlation and sensitivity analysis was carried out. In summary of the analysis findings, it can be stated that significant correlation were observed, for the selected FOMs, with the following uncertain-parameters: *power in the bundle*, *steam mass flow rate, electric power*, *instant of quenching injection*, *threshold void fraction to allow exchange with liquid droplets*. The analysis findings represents a feedback on how to reduce code uncertainty in future studies.

CRediT authorship contribution statement

Pietro Maccari: Conceptualization, Software, Formal analysis, Investigation, Data curation, Writing – original draft, Writing – review & editing, Visualization. **Andrea Bersano:** Resources, Writing – review & editing, Methodology, Formal analysis, Validation. **Stefano Ederli:** Supervision, Investigation, Validation, Software. **Fabrizio Gabrielli:** Resources, Supervision, Project administration, Writing – review & editing, Conceptualization. **Fulvio Mascari:** Conceptualization, Methodology, Investigation, Resources, Writing – review & editing, Validation, Supervision, Project administration.

Declaration of Competing Interest

The authors declare that they have no known competing financial interests or personal relationships that could have appeared to influence the work reported in this paper.

Data availability

The authors do not have permission to share data.

Acknowledgements

This research is supported by the International Atomic Energy Agency under the Coordinated Research Project award I31033 on Advancing the State-of-Practice in Uncertainty and Sensitivity Methodologies for Severe Accident Analysis in Water Cooled Reactors, launched in 2019. The authors gratefully acknowledge IRSN for their valuable comments and suggestions during the preparation of the manuscript.

References

A. Alfonsi, et al., "RAVEN Theory Manual", INL/EXT-16-38178, Idaho National Laboratory (INL), 2020.
Ambrosini, W., et al., 1990. Evaluation of accuracy of thermal hydraulic code calculation. Energia Nucleare (Rome) 7 (2), 5–16.
Baccou, J., et al., 2020. SAPIUM: A generic framework for a practical and transparent quantification of thermal-hydraulic code model input uncertainty. Nucl. Sci. Eng. 194 (8–9), 721–736.
A. Bersano, F. Mascari, M. T. Porfiri, P. Maccari, and C. Bertani, "Ingress of coolant event simulation with trace code with accuracy evaluation and coupled DAKOTA uncertainty analysis," Fusion Eng. Des., vol. 159, p. 111 944, 2020.
S. Brumm, et al., Status of the uncertainty quantification for severe accident sequences of different NPP designs in the frame of the H-2020 project MUSA, In The 10th European Review Meeting on Severe Accident Research (ERMSAR2022), Karlsruhe, Germany, 2022. https://musa-h2020.eu/wp-content/uploads/2022/07/ERMSAR2022_PAPER_278_WP5_V1.pdf.
Carénini, L., Fleurot, J., Fichot, F., 2014. Validation of ASTEC V2 models for the behaviour of corium in the vessel lower head. Nucl. Eng. Des. 272, 152–162.
Chatelard, P., Reinke, N., Arndt, S., et al., 2014. ASTEC V2 severe accident integral code main features, current V2.0 modelling status, perspectives. Nucl. Eng. Des. 272, 119–135.
Chatelard, P., Belon, S., Bosland, L., et al., 2016. Main modelling features of the ASTEC V2.1 major version. Ann. Nucl. Energy 93, 83–93. https://doi.org/10.1016/j.anucene.2015.12.026.
Coindreau, O., et al., 2023. Uncertainty quantification for a severe accident sequence in a SFP in the frame of the H-2020 project MUSA: First outcomes. Ann. Nucl. Energy 188, 109796.
F. S. D'Auria, H Glaeser, S Lee, J Mĺak, M Modro, and R. Schultz, "Best Estimate Safety Analysis for Nuclear Power Plants: Uncertainty Evaluation." IAEA Safety Report Series. International Atomic Energy Agency (IAEA), vol. 52. 2008.
D'Auria, F., Frogheri, M., Giannotti, W., 1999. RELAP/MOD3.2 Post Test Analysis and Accuracy Quantification of SPES Test SP-SB-04. NUREG/IA-0155.
"LLC, Transmittal Document for MAAP5 Code Revision MAAP 5.02," Fauske & Associates, FAI/13-0801, 2013.
Gabrielli, F., Sanchez-Espinoza, V.H., Stuckert, J., Gomez Garcia-Torano, I., March 18–20, 2019.. Validation of the ASTEC Integral Code using the QUENCH-06 and QUENCH-08 Experiments. Proc. of the 9th European Review Meeting on Severe Accident Research (ERMSAR2019). Prague, Czech Republic.
Glaeser, H., 2008. GRS method for uncertainty and sensitivity evaluation of code results and applications. Sci. Technol. Nucl. Install.
Gómez-García-Toraño, I., Laborde, L., 2021. Modelling reflooding of intact core geometries in ASTEC V2. 1: Improvements and validation on PERICLES experiments. Nucl. Eng. Des. 378, 111157. https://doi.org/10.1016/j.nucengdes.2021.111157.
Goodfellow, I., Bengio, Y., Courville, A., 2016. Deep learning. MIT Press.
Guba, A., Makai, M., Pàl, L., 2003. Statistical aspects of best estimate method—I. Reliab. Eng. Syst. Saf. 80 (3), 217–232.
Herranz, L.E., Beck, S., Sanchez-Espinoza, V.H., Mascari, F., Brumm, S., Coindreau, O., Paci, S., 2021. The EC MUSA Project on Management and Uncertainty of Severe Accidents: Main Pillars and Status. Energies 14.
https://www.iaea.org/projects/crp/i31033.
L. L. Humphries, V. G. Figueroa, M. F. Young, D. Louie, and J. T. Reynolds, "MELCOR Computer Code Manuals," Sandia National Lab.(SNL-NM), Albuquerque, NM (United States), SAND-2015-6692R, 2015. doi: 10.2172/1433918. https://www.osti.gov/biblio/1433918.
Kaliatka, A., Vileiniškis, V., Uŝpuras, E., 2014. Modelling of QUENCH-03 and QUENCH-06 experiments using RELAP/SCDAPSIM and ASTEC codes. Sci. Technol. Nucl. Install. https://doi.org/10.1155/2014/849480.
Maccari, P., et al., 2021. ASTEC-RAVEN coupling for uncertainty analysis of an ingress of coolant event in fusion plants. Fusion Eng. Des. 169, 112442.
Mascari, F., et al., 2022. "First outcomes from the PHEBUS FPT1 uncertainty application done in the EU-MUSA project", In The 19th International Topical Meeting on Nuclear Reactor thermal Hydraulics (NURETH-19). Belgium, Brussels https://musa-h2020.eu/wp-content/uploads/2022/07/35666_V1.pdf.
Mascari, F., De Rosa, F., Nakamura, H., Umminger, K., D'Auria, F.S., 2015. Scaling issues for the experimental characterization of reactor coolant system in integral test facilities and role of system code as extrapolation tool. In: Proceedings of 16th International Topical Meeting on Nuclear Reactor Thermal-Hydraulics (NURETH-16). American Nuclear Society, pp. 4921–4934.
F. Mascari, et.al., Overview of IAEA CRP I31033 "Advancing the state-of-practice in uncertainty and sensitivity methodologies for severe accident analysis in water cooled reactors", The 10th European Review Meeting on Severe Accident Research (ERMSAR2022), Akademiehotel, Karlsruhe, Germany, May 16-19, 2022.
F. Mascari, A. Bersano, G. Agnello, M. Angelucci, J. Phillips, D. Luxat, "MELCOR – DAKOTA Coupling for Uncertainty Analyses, in a SNAP Environment/Architecture", NUREG/IA-0532, 2023. https://www.nrc.gov/reading-rm/doc-collections/nuregs/agreement/ia0532/index.html.
OECD/NEA/CSNI, 2007, BEMUSE Phase III Report: Uncertainty and Sensitivity Analysis of the LOFT L2-5 Test, NEA/CSNI/R(2007)4.
OECD/NEA/CSNI, 2011, BEMUSE Phase VI Report: Status Report on the Area, Classification of the Methods, Conclusions and Recommendations, NEA/CSNI/R (2011)4.
OECD/NEA/CSNI, 2016, PREMIUM: A Benchmark on the Quantification of the Uncertainty of the Physical Models in the System Thermal-hydraulic Codes. Methodologies and Data Review, NEA/CSNI/R(2016)9.
Perez, M., et al., 2011. Uncertainty and sensitivity analysis of a LBLOCA in a PWR Nuclear Power Plant: Results of the Phase V of the BEMUSE programme. Nucl. Eng. Des. 241 (10), 4206–4222.
Prošek, A., et al., 2002. Review of quantitative accuracy assessments with fast Fourier transform based method (FFTBM). Nucl. Eng. Des. 217 (1–2), 179–206.
Prošek, A., et al., 2008. Quantitative assessment with improved fast Fourier. Nucl. Eng. Des. 238, 2668–2677.

Prošek, A., et al., 2015. Use of FFTBM by signal mirroring for sensitivity study. Ann. Nucl. Energy 76, 253–262.
A. Prošek, et.al. "Application of FFTBM to Severe Accidents", Proceedings of Nuclear Energy for New Europe, Bled, Slovenia, 2005.
A. Prošek, "JSI FFTBM Add-In 2007 User's Manual", IJS-DP-9752, 2007.
Rossum, V., 1995. Python reference manual. Centrum voor Wiskunde en Informatica, Amsterdam.
L. Sepold, W Hering, C Homann, et al., "Experimental and computational results of the QUENCH-06 test (OECD ISP-45)," Forschungszentrum Karlsruhe GmbH Technik und Umwelt (Germany), FZKA-6664, 2004.
Wald, A., 1943. An extension of Wilks' method for setting tolerance limits. Ann. Math. Stat. 14 (1), 45–55.
Wilks, S.S., 1941. Determination of sample sizes for setting tolerance limits. Ann. Math. Stat. 12 (1), 91–96.
Wilks, S.S., 1942. Statistical prediction with special reference to the problem of tolerance limits. Ann. Math. Stat. 13 (4), 400–409.